TU Delft

Delft University of Technology

Document Version
Final published version

Licence
CC BY

Citation (APA)
Grenko, B., van Biert, L., van de Ketterij, R., & de Jong, W. (2026). Experimental validation of a dynamic 2D model for catalytic methanol steam reforming in a fixed bed reactor. *Chemical Engineering Journal*, *545*, Article 179613. https://doi.org/10.1016/j.cej.2026.179613

Important note
To cite this publication, please use the final published version (if applicable).
Please check the document version above.

Copyright
In case the licence states “Dutch Copyright Act (Article 25fa)”, this publication was made available Green Open Access via the TU Delft Institutional Repository pursuant to Dutch Copyright Act (Article 25fa, the Taverne amendment). This provision does not affect copyright ownership.
Unless copyright is transferred by contract or statute, it remains with the copyright holder.

Sharing and reuse
Other than for strictly personal use, it is not permitted to download, forward or distribute the text or part of it, without the consent of the author(s) and/or copyright holder(s), unless the work is under an open content license such as Creative Commons.

Takedown policy
Please contact us and provide details if you believe this document breaches copyrights.
We will remove access to the work immediately and investigate your claim.

This work is downloaded from Delft University of Technology.

Chemical Engineering Journal 545 (2026) 179613

Contents lists available at ScienceDirect

Chemical Engineering Journal

journal homepage: www.elsevier.com/locate/cej

Experimental validation of a dynamic 2D model for catalytic methanol steam reforming in a fixed bed reactor

Bojan Grenko [a,*], Lindert van Biert [a], Robert van de Ketterij [b], Wiebren de Jong [c]

[a] Maritime Transport and Technology Department, Delft University of Technology, Mekelweg 2, Delft, 2628 CD, The Netherlands
[b] Military Technological Sciences Department, Netherlands Defence Academy, Het Nieuwe Diep 8, Den Helder, 1781 AC, The Netherlands
[c] Process and Energy Department, Delft University of Technology, Leeghwaterstraat 39, Delft, 2628 CB, The Netherlands

ARTICLE INFO

Keywords:
Methanol steam reforming
Validation
2D dynamic
Modelling
Experimental
Fixed bed

ABSTRACT

The growing adoption of renewable power in the chemical processing industry shifts many processes into the dynamic operating regime. The common 1D reactor models used for process design are no longer necessarily adequate for representing transient operation. In this study, a 2D pseudo-homogeneous dynamic model of a fixed bed reactor is developed and validated using methanol steam reforming as focused case. The model is experimentally validated with combined measurements of reactor bed temperature and outlet carbon monoxide concentration in time. The study found that the 2D model matches well in values and trends with experimental data despite numerous parameter uncertainties and use of standard equations from the literature. The largest influence on model prediction was found in external practical heating non-uniformities, such as heat losses and added heat capacity of the reactor support structure. The non-uniformities can cause up to 20% change in CO concentration predicted at the outlet, and double the transient time in certain cases. The model captures well the reactor transient characteristics well, and is regarded fit for design of reactors in the unsteady operating regime.

1. Introduction

One of the outcomes of defossilization objectives is an increased necessity for alternative chemical conversion processes. In the short term, various waste management [1,2], exhaust aftertreatment technologies [3], and carbon capture are needed [4,5]. The long term solution appears to be large scale chemical storage of renewable energy [6,7]. The choice of the produced energy carrier depends on required physico-chemical properties and available feedstock. It is therefore likely that various combinations and processes are the answer for the long term energy supply sustainability [6]. The subsequent energy conversion via appropriate fuel processing is then envisioned near the end user. Given the variation in renewable energy supply and demand, dynamic on-demand processing expectedly becomes commonplace.

The hydrogen economy is an often proposed model of a future renewable energy system [8]. The efficient conversion of hydrogen to electrical power has already been established through the use of fuel cells, and their potential application is wide [9–11]. In this foreseen future, hydrogen carriers are envisioned for alleviating situations with problematic energy storage and transport [12,13].

Methanol is one of the promising candidates for early wide adoption as hydrogen carrier due to its liquid state at ambient conditions, current availability, established production chains, and demonstrated possibility for sustainable synthesis [12]. The foundations for methanol to hydrogen conversion have already been laid down, and research lately often focuses on the fuel cell-based system level concepts [14–16]. The benefits of methanol-to-fuel cell power generation systems include it being a high energy density fuel, resulting in potentially no harmful emissions. These characteristics are highly valuable in transport applications such as maritime transport [17].

The variable power demand in particularly maritime transport requires design of components for the unsteady regime. The common 1D models used for steady state design generate conversion and selectivity errors in transient regimes, as already concluded by a previous analysis [18]. The analysis shows that the traditional design approach for a transport setting consequently mispredicts system performance characteristics during each power demand adjustment. Moreover, the selectivity misprediction in transients could significantly affect the lifetime of processing components in a PEMFC-based systems, which have strict requirements of H_2 purity and allowed CO content. The analysis also concludes an expectedly increased necessity for dynamic models and procedures.

The 3D fixed bed reactor models are also unfit for design for the unsteady regime, due to the required computational effort [19–21].

* Corresponding author.
E-mail address: b.grenko@tudelft.nl (B. Grenko).

https://doi.org/10.1016/j.cej.2026.179613
Received 23 March 2026; Received in revised form 11 June 2026; Accepted 16 July 2026
Available online 23 July 2026
1385-8947/© 2026 The Authors. Published by Elsevier B.V. This is an open access article under the CC BY license (http://creativecommons.org/licenses/by/4.0/).

Such 3D models tend to prioritize accuracy and resolve many of the flow characteristics. Overly high fidelity is limiting to the reactor design tasks due to the iterative nature, which is especially problematic in dynamic simulations. Designing a reactor for dynamic operation requires a model balanced for accuracy and computation time, which is a relatively new objective in the chemical process engineering literature.

In this work, a dynamic 2D pseudo-homogeneous model for methanol reforming in a fixed bed reactor is presented. This mid-fidelity model is proposed as a balance in computational effort and accuracy with characteristics in between a 1D and a 3D model. A newly designed experimental setup is used for obtaining reference validation data. Several heating non-uniformities present in the experiments are shown to have a large influence on the overall process. It is therefore recommended that the design procedure accounts for details such as heat losses and heat capacity of the support structures, if possible. The model is validated in steady and unsteady state through measurements of internal bed temperature and carbon monoxide content in the reformate. These measurements directly and indirectly validate reaction rates, heat and mass transfer, and heat consumption in time within the bed. Some model uncertainty stems from the used semi-empirical equations. The transient performance is found mostly affected by parameters such as heat capacity. The simulations agree with measurements in time and ultimately the model is concluded fit for reactor design tasks in the transient regime.

1.1. Methanol steam reforming

Methanol steam reforming is the most commonly utilized conversion method for supplying fuel cells with hydrogen [22–26]. Additionally, steam reforming has the highest hydrogen yield and best CO selectivity among methanol conversion methods [27], which is especially favoured when combined with PEM fuel cells. The dominant reactions in methanol steam reforming (MSR) are the (i) methanol steam reforming reaction:

$$CH_3OH + H_2O \rightleftharpoons CO_2 + 3\,H_2 \qquad \Delta H^0_{298} = 49.4\,\text{kJ/mol}, \tag{1}$$

(ii) the water-gas shift (WGS):

$$CO + H_2O \rightleftharpoons CO_2 + H_2 \qquad H^0_{298} = -41.1\,\text{kJ/mol}\quad , \tag{2}$$

and the (iii) methanol decomposition (MD):

$$CH_3OH \rightleftharpoons CO + 2\,H_2 \qquad H^0_{298} = 90.5\,\text{kJ/mol}\quad . \tag{3}$$

The reforming process is overall endothermic. The methanol conversion can occur either directly through MSR, or indirectly through MD followed by the WGS reaction. Large reactors are often constructed as shell and tube heat exchangers [28,29] (see Fig. 1). Flue gas or steam are generally used as shell side heat supply medium [29], but electrically heated reactors are also emerging recently [30]. Catalysts for the process are often copper based, the most common commercial one being $CuO/ZnO/Al_2O_3$. Alternatively, Palladium based catalysts appear promising based on their CO selectivity [31]. However, they are still confined to research settings at present time.

2. Experimental methods

This section presents the designed experimental setup for unsteady methanol reforming validation. Material properties of the reactor and catalyst are reported, and experimental preparation procedures are explained. Then, the validation approach through performed measurements is described. Finally, the experimental uncertainties are identified and their assessment reported.

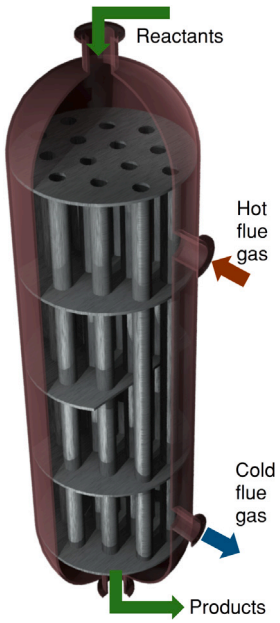

Fig. 1. Methanol steam reforming reactor as shell and tube heat exchanger heated with flue gas.
Source: Reprinted from [32] with permission of Elsevier, Copyright 2025.

2.1. Experimental equipment and materials

An experimental setup is designed for dynamic operation and measurements in a packed bed methanol steam reformer. The setup schematic (Fig. 2) shows an overview of the process, equipment, and their control integration. The inlet feed, which can be either methanol or a gas mixture, is pre-heated in the evaporator before entering the reactor. The process is monitored with temperature sensors inserted in the packed bed. The reactor back pressure is controlled with a diaphragm valve. The outlet stream is condensed, sampled, and analysed using a gas chromatograph, and then vented.

The equipment is connected to a desktop PC either directly or via PLC, and it is controlled through LabView environment. A Gilson 305 high-performance liquid chromatography (HPLC) pump module precisely regulates the flow rate of liquid reactants. The reactants are then evaporated in a pipe section with a surrounding trace heating cable (P_{max}=1250 W), and their temperature at the reactor inlet is controlled by a feedback loop using a thermocouple in the inert inlet zone of the reactor filled with alumina particles of 1.5 mm average diameter. Another trace heating wrapped around the reactor supplies the reaction heat (P_{max}=1600 W), and the external wall temperature is regulated with a thermocouple positioned at the contact area of the trace heating and the reactor. The pressure is controlled with a back pressure regulator placed directly after the reactor. A Pressure Control Solutions EQ-DA smart pilot pneumatic actuator controls the outlet pressure through an Equilibar dome loaded control valve, and is used as closed loop controller with the reference pressure reading from inlet or outlet pressure sensors. In addition to temperature and pressure, the gas composition is analysed using an Agilent Micro gas chromatograph (GC). The GC uses Argon as a carrier gas, and has two columns heated at 373 K: 1 m column with Cox heated injector, and a 4 m column with 5CB heated injector.

The reactor is made from Inconel 600 alloy material. Reactor material properties and dimensions are reported in Table 1. The internal surfaces in contact with hot reactants or products are coated with SilcoNert2000 inert coating to minimize side reactions. The coated surfaces include the reactor pipe, evaporator pipe, and all temperature and pressure sensors areas directly in contact with the flow. The reactor

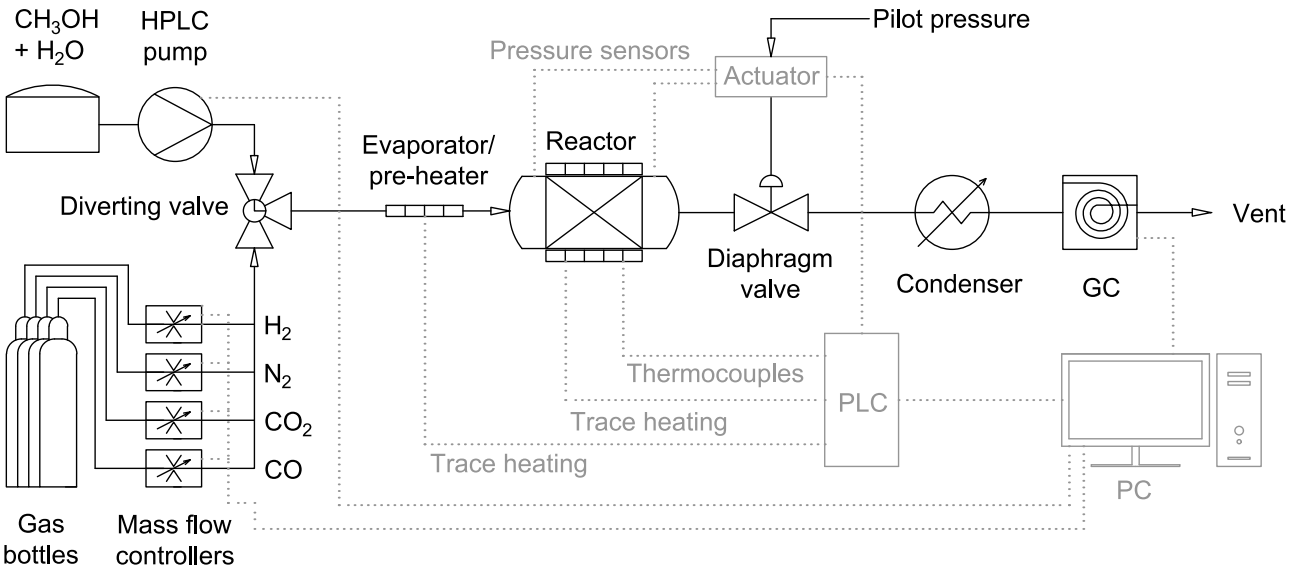

Fig. 2. Schematic of the experimental methanol steam reforming setup.

Table 1
Properties of reactor tube made from Inconel 600.

Parameter	Value	Description
d_{in} [mm]	30	Reactor internal diameter
s_w [mm]	5	Reactor wall thickness
l_r [mm]	300	Reactor length (active region)
$c_{p,w}$ (J kg^{-1} K^{-1})	444	Tube wall specific heat capacity
k_w [W m^{-1} K^{-1}]	14.9	Thermal conductivity of reactor wall
ρ_w (kg m^{-3})	8470	Density of the reactor wall

is vertically mounted to ensure downward reactant flow, as shown in the setup photograph in Fig. 3.

The reactor contains 36 temperature sensors and 2 pressure sensors. The sensors are placed in the fixed bed according to Fig. 4. The thermocouples (TCs) are distributed across 11 inserts consisting of single point, 5-point, and 2-point sensors. One single point sensor is inserted in the inert inlet zone to monitor and control the reactant inlet temperature. Five 5-point sensors are placed at the start of the active zone, where a high temperature gradient is expected. In 5-point sensors, the TCs are uniformly spaced 5 mm from each other and the reactor wall. In 2-point sensors, one TC is placed 5 mm away from the wall opposite to the insert point, and the other at the reactor centreline. The axial positions of all temperature sensor inserts are given in Table 2. The two pressure sensors are placed at the boundaries of the active catalyst zone, annotated with A and B in Fig. 4.

The designed reactor is filled with inert pellets and active catalyst pellets according to the schematic shown in Fig. 4. The reactor is divided into three zones in the axial direction: inert inlet, active middle, and inert outlet zone. The surrounding inert zones ensure that the gas flow in the active catalyst zone is not affected by pipe diameter variations at the inlet and outlet. The reactor total length is 450 mm, where the inert inlet zone is 100 mm, the active catalyst zone is 300 mm, and the inert outlet zone is 50 mm long. The packing zone interfaces are separated with quartz filters to prevent mixing.

The commercially available $CuO/ZnO/Al_2O_3$ cylindrical catalyst pellets supplied by Shandong Dengzhuo Chemical Co., Ltd with 40/40/20 wt% composition are used in the experiments. The pellets are crushed and sieved to 1 mm < d_p < 2 mm size fraction before loading them in the reactor. This way, approximately 20 pellets fit across the reactor diameter which minimizes the wall effects on the internal gas flow [33]. The reactor is filled with 0.296 kg of crushed catalyst. The resulting bulk density is ρ_b = 1396 kg m^{-3}, and bed porosity is ε = 0.39. The crushed catalyst surface area and average pore radius are obtained through measurements using an Anton Paar® Autosorb 6100 high vacuum physisorption analyser. The complete list of catalyst properties is reported in Table 3.

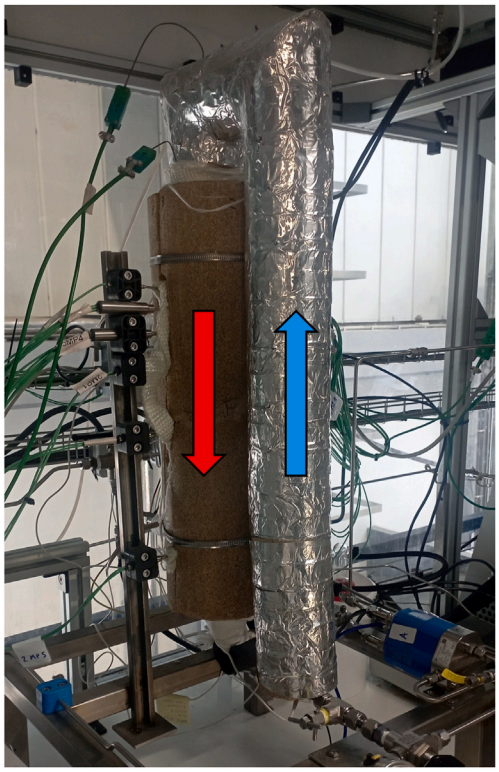

Fig. 3. Methanol steam reforming reactor vertically mounted for downward fluid flow (red arrow), and evaporator/pre-heater pipe leading up to the reactor top inlet with upward fluid flow (blue arrow).

Prior to the experiments, the catalyst was activated with a hydrogen and nitrogen mixture in equal molar ratios through the reactor. The flow of 300 standard ml/min and reactor temperature of 500 K were maintained at ambient pressure during the activation. The flow was kept relatively low to regulate the exothermic activation reaction and

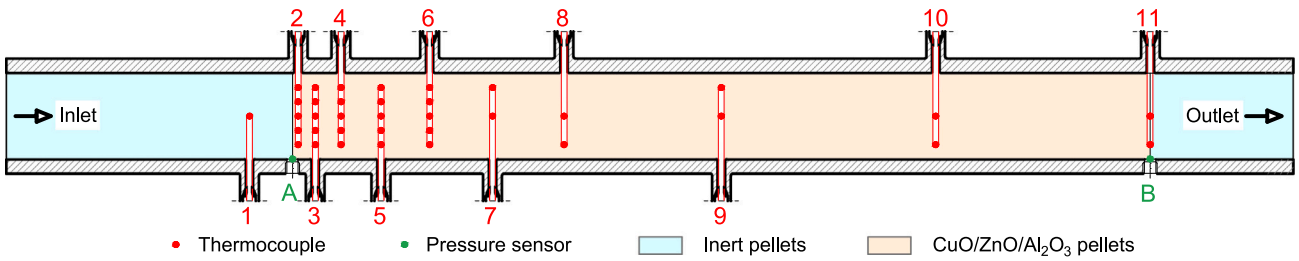

Fig. 4. Schematic of the cross section reactor tube showing flow direction, reactor packing zones, and thermocouple and pressure sensor placement within the reactor.

Table 2
Positions of temperature sensor inserts in the methanol steam reforming reactor.

Insert number	1	2	3	4	6	5	7	8	9	10	11
Rel. distance from active zone interface [mm]	−15	2	8	17	48	31	70	95	150	225	300
No. of TC sensors in the insert	1	5	5	5	5	5	2	2	2	2	2

Table 3
Properties of the crushed commercial $CuO/ZnO/Al_2O_3$ catalyst pellets used in the experiments.

Parameter	Value	Description
d_p [mm]	1.5	Catalyst pellet average diameter
ρ_c [kg m^{-3}]	1396	Catalyst bulk density
$\rho_{c,s}$ [kg m^{-3}]	2293	Catalyst material density
ϵ [–]	0.39	Bed porosity
$c_{p,s}$ [J kg^{-1} K^{-1}]	950	Catalyst specific heat capacity
S_c [m^2 kg^{-1}]	$118 \cdot 10^3$	Catalyst BET surface area
d_{pore} [Å]	247	Catalyst average pore diameter

keep the catalyst below the sintering temperature of ~570 K. The activation procedure was completed after the axial temperature profile was stable, which took about 10 h.

2.2. Data gathering approach

Two experimental techniques are used for steady state validation: temperature measurements and gas analysis. The thermocouple inserts presented in Fig. 4 relay axial and radial temperature gradients. The temperature profile is a result of external heat supply, axial and radial transport, and heat consumption by the reactions. A comparable temperature field from the model is achieved when all heat fluxes are correctly captured.

Outlet methanol conversion cannot be directly measured since the used gas chromatograph requires dry gas. Only the relative concentrations of H_2, CO_2, and CO can be measured.

The CO concentration measurement is used as conversion indicator since CO content is inversely proportional to the methanol conversion. As methanol is converted, the local bed temperatures rise due to lower reaction rates of MSR and MD (Eqs. (1), (3)). The equilibrium then shifts and the reverse WGS (Eq. (2)) produces CO. Thus CO concentration measurements are used in place of methanol conversion for validation.

For dynamic analysis, the gas chromatograph is run continuously and generates data points at ≈4 min intervals. The gas residence time in the tubes leading to the GC has not been determined. However, the data points indicate a trend that can be captured by the model.

2.3. Experimental uncertainties and non-uniformities

Several uncertainties and non-uniformities are present in the experimental part of the study. Each uncertainty impacts the validation in a different way since they stem from various sources. The major concerns and their treatments are described here.

Crushed and sieved catalyst has irregular shapes and non-uniform pellet sizes. In the modelling equations, however, an average value of catalyst diameter (d_p = 1.5 mm) must be used. The pellet volume and macro surface area are calculated using equations for a spherical catalyst with equivalent diameter. These parameters are used in expressions for effective radial transport, heat transfer coefficient, and pressure drop. The isolated effects of the used catalyst shapes would have to be explored in a dedicated experimental study. In the present work, the affected expressions are observed within a sensitivity study shown in the *Numerical model* section.

Deviations from ideal behaviour on the reactor bed scale are also observed. Over the course of the first ≃50 h of operation the bed activity slowly decreased, after which it settled. The decrease was observed indirectly with temperature measurements. The inlet zone is found most affected by the decrease, for multiple likely reasons. First, possible bed settling shifts material away from the inlet in the vertically installed reactor. Second, the expected initial activity decreases due to sintering or pore clogging. Third, the inlet zone has less catalyst due to dense thermocouple placement. This can reinforce the activity decrease from settling.

The converged activity state is seen in Fig. 5 through a rapid decrease in temperature at the thermocouple insert at position 5. This decrease is generally expected at the initial contact of reactants with the catalyst. This effect is included in the model, and is explained in detail in the *Numerical model* section.

The effects of thermal conduction through the thermocouple inserts are investigated under steady state reforming conditions with 5-point inserts, as shown in Fig. 5. The accuracy of the used K-type thermocouples is ± 2.5 K, so only higher gradients are used to draw conclusions. All steady states show similar behaviour like the process conditions reported in Fig. 5.

The inserts numbered 2–4 in the low activity area indicate heat conduction away from the thermocouple with a gradient of up to 10 K across between sensors *a* and *e*. Inserts 5 and 6 are in an active heat transfer limited zone. The sensors *a-c* have a low gradient between them in all cases, which implies that conduction along the sensor is not dominant over heat exchange with the bed packing in this region. The conduction may still be present, but it is concluded tolerable. Therefore only sensors *a-c* are used for validation. The conduction is assumed to be the same for 2-point inserts, which have only *a* and *c* sensor positions, both of which are used in the validation.

Finally, several imperfections are present in reactor heating, such as heat losses, trace heater wrapping non-uniformity, the inlet reactant

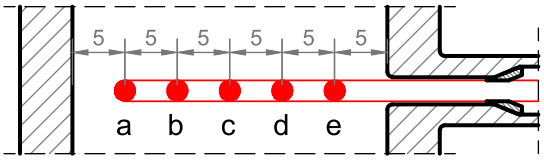

(a) Thermocouple sensor names in a 5-point insert relative to the point of insertion and gas-tight ferrule seal. Dimensions are drawn in mm.

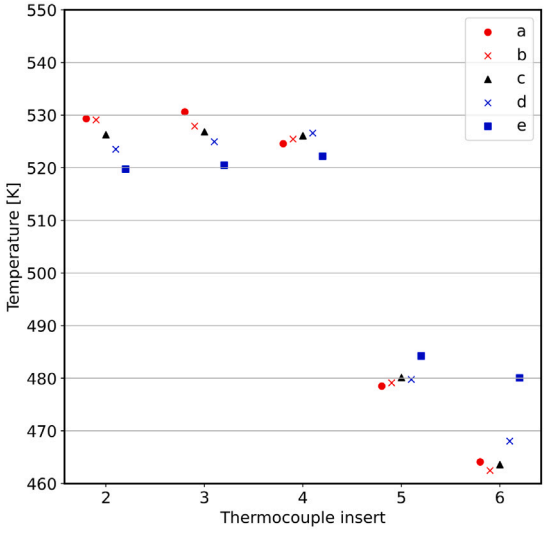

(b) P = 150 W; $W_{cat.}/F_{CH_3OH}$ = 200 kg mol s^{-1}

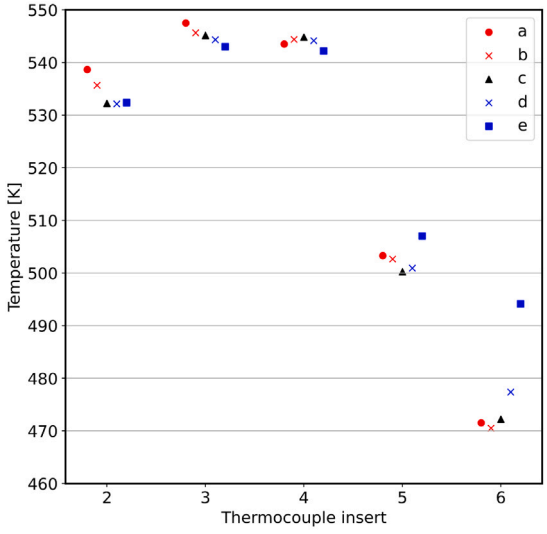

(c) P = 224 W; $W_{cat.}/F_{CH_3OH}$ = 150 kg mol s^{-1}

Fig. 5. Temperature measurements from 5 point thermocouple inserts during two selected steady reforming operations with specified electric power input and methanol inlet flow at steam-to-carbon molar ratio of S/C = 1.5.

temperature control, the reactor bed activity changes after stabilization, and variable heat capacity of the reactor due to its mounting. All these effects are quantified, addressed a posteriori in the model, and their effect is presented in the *Numerical methods* section.

3. Numerical methods

The present model is created by extending the steady state 2D model of Zhu et al. [34–36], formulated in cylindrical coordinates. The newly developed model is open source and available from a git repository [37]. The formulae for terms not presented in the main text can be found in the supplementary material, and the original publications of Zhu et al. The mass and energy equations of an unsteady pseudo-heterogeneous model used in the present study are:

$$\varepsilon \frac{\partial C_i}{\partial t} = -u_s \frac{\partial C_i}{\partial z} + D_{er}\left(\frac{\partial^2 C_i}{\partial r^2} + \frac{1}{r}\frac{\partial C_i}{\partial r}\right) + \rho_c r_i, \tag{4}$$

$$\left(\varepsilon \rho_f c_{p,f} + (1-\varepsilon)\rho_s c_{p,s}\right)\frac{\partial T}{\partial t} = -u_s \rho_f c_{p,f}\frac{\partial T}{\partial z} + \lambda_{er}\left(\frac{\partial^2 T}{\partial r^2} + \frac{1}{r}\frac{\partial T}{\partial r}\right) + \sum \eta_j \rho_c \left(-\Delta H_j\right) r_j S_c \tag{5}$$

where ε (-) is the bed porosity, C_i (mol m^{-3}) are the species concentrations, u_s (m s^{-1}) is the flow superficial velocity, D_{er} (m^2 s^{-1}) is the effective radial dispersion coefficient, ρ_c (kg m^{-3}) is the catalyst bulk density, r_i (mol s^{-1} m^{-2}) is the formation/consumption rate of component i, $c_{p,f}$ (J kg^{-1} K^{-1}) is the fluid (gas) phase specific heat capacity, $\rho_{c,f}$ (kg m^{-3}) is the fluid (gas) phase density, $c_{p,s}$ (J kg^{-1} K^{-1}) is the solid phase specific heat capacity, $\rho_{c,s}$ (kg m^{-3}) is the solid phase (catalyst material) density, T (K) is the temperature, λ_{er} (W m^{-1} K^{-1}) is the effective radial thermal conductivity, η_j are the effectiveness factors evaluated per reaction j, ΔH_j (J mol^{-1}) is the reaction enthalpy

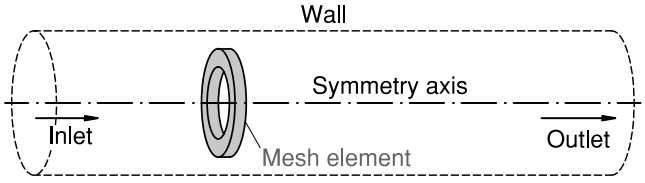

Fig. 6. Illustration of reactor tube domain boundaries and mesh element in cylindrical coordinates.

of reaction j, r_j (mol s^{-1} m^{-2}) is the reaction rate of reaction j, and S_c (m^{-2} kg^{-1}) is the catalyst BET surface area. The formulas for η_j calculated with Thiele modulus (approach validated by Zhu et al. [38]), D_{er}, and λ_{er} are shown in the supplementary material.

Axial dispersion terms are not included in this model for computational efficiency. Axial effects are not dominant in flows with high Péclet numbers according to Sahimi et al. [39]. In the present work, Péclet numbers are always higher than 240, which falls under the regime as *dominated by convective transport* according to Sahimi. Above Pe = 300, the regime becomes *purely convective*.

The simulation domain and representative mesh element shape for cylindrical coordinates are shown in Fig. 6. The boundary condition equations are given in Table 4.

The energy conservation equation of the reactor tube wall is:

$$\rho_w c_{p,w}\frac{\partial T_w}{\partial t} = k_w \frac{\partial T_w^2}{\partial^2 z} + \frac{P_{el,in} * \eta_d}{V_t} - Q_{loss}\frac{A_{t,in}}{V_t} + U\Delta T_{w,r}\frac{A_{t,in}}{V_t}, \tag{6}$$

where ρ_w (kg m^{-3}) is the reactor wall material, $c_{p,w}$ (J kg^{-1} K^{-1}) is the reactor wall material specific heat capacity, T_w (K) is the wall temperature, k_w (W m^{-1} K^{-1}) is the thermal conductivity of reactor

Table 4
Simulation boundary conditions.

Position	Coordinates	Boundary condition
Inlet	$z = 0$ $0 \le r \le r_{max}$	$C_i = C_{in}$ $T = T_{in}$
Outlet	$z = z_{max}$ $0 \le r \le r_{max}$	$\frac{\partial C_i}{\partial z} = 0$ $\frac{\partial T}{\partial z} = 0$
Wall	$0 \le z \le z_{max}$ $r = r_{max}$	$\frac{\partial C_i}{\partial r} = 0$ $\frac{\partial T}{\partial r} = -\frac{U}{\lambda_{er}}(T_{wall} - T)$
Symmetry axis	$0 \le z \le z_{max}$ $r = 0$	$\frac{\partial C_i}{\partial r} = 0$ $\frac{\partial T}{\partial r} = 0$

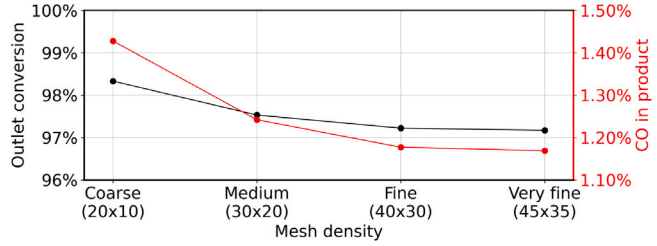

Fig. 7. Grid convergence study with outlet methanol conversion and CO content for P = 187 W, $W_{cat.}/F_{CH_3OH}$=200 kg s mol^{-1} case.

wall material, $P_{el,in}$ (W) is the electric trace heater power, η_d (-) is the trace heater wrapping density (heat generation) factor, Q_{loss} (W m^{-2}) is the area normalized heat loss, U (W m^{-2} K^{-1}) is the combined heat transfer coefficient, $\Delta T_{w,r}$ (K) is the temperature difference between tube wall and reactants, $A_{t,in}$ (m^2) is the inner surface area of one reactor tube, and V_t (m^3) is the reactor tube wall volume. The external heating is thus applied to the reactor through the tube wall energy equation.

The overall heat transfer coefficient U (W m^{-2} K^{-1}) includes resistances from the tube side gas film and within the reactor tube wall. It is calculated according to:

$$U = \left(\frac{1}{h_t} + \frac{s_w}{k_w} \frac{d_{t,out}}{d_{lm}} \right)^{-1}, \tag{7}$$

The used kinetics model has been developed by Peppley et al. [40] for a commercial CuO/ZnO/Al_2O_3 catalyst. The equations are shown in the supplementary material. The kinetic model is based on a Langmuir-Hinshelwood mechanism for surface reactions, and includes the three reversible dominant reactions of MSR described in Eqs. (1)–(3). The pressure losses along the reactor bed are calculated with the semi-empirical model of Ergun [41].

3.1. Numerical schemes and discretization

A second order upwind scheme is used for advection terms, while a 4th order central differencing scheme is used for the radial terms. Before each unsteady simulation, a steady state is initialized until mass and energy balances converge to residuals below 10^{-5}. A Runge–Kutta 4th order scheme is used for temporal evolution in the unsteady simulation. A constant unsteady timestep of $4 \cdot 10^{-4}$ seconds was used based on the rates of reaction. The simulated domain is discretized with a uniform mesh with 45 axial and 30 radial cells. Fig. 7 shows the results of a grid convergence study.

3.2. Parameter sensitivity study

Parameters with potentially high impact on the results are investigated in a sensitivity study. Effective radial coefficients for dispersion (D_{er}) and thermal conductivity (λ_{er}) are chosen due to their large role in radial transport terms. The tube side heat transfer coefficient (h_t) is included because of expected impact on radial heat transport. Finally, the pressure drop (Δ_p) is included due to its potential impact on reaction rates.

The sensitivity analysis of the described parameters was conducted by multiplying the result of their respective equations, presented in the supplementary material, with factors of 0.25, 0.5, 2, and 4. The factor variation impact is characterized by methanol conversion, and CO concentration at the outlet. The sensitivity study in Fig. 8(a) shows that scaling the radial heat transfer parameters, λ_{er} and h_t has the highest influence on conversion and selectivity.

As introduced in Section 2.3, the crushed catalyst pellets are not uniform in size in the present experiments. An averaged value of catalytic pellet diameter d_p is used in the model, namely in the formulas for D_{er}, λ_{er}, h_t, and Δ_p. Further analysis is conducted on the impact of d_p variations within the selected parameters.

The average value of d_p was also scaled by the factors of 0.25, 0.5, 2, and 4 within the expressions for the two most sensitive parameters λ_{er} and h_t. Results of this analysis in Fig. 8(b) show a mild effect through λ_{er}, while h_t is sensitive to pellet size changes.

The size range of experimental catalyst pellets is relatively small compared to the investigated range. The sieved catalyst sizes range between 1 and 2 mm, which is 67% and 175% deviation respectively of the average 1.5 mm value. The d_p variation has a negligible influence through λ_{er} in the present study. A larger effect is seen in h_t manipulation. Based on the results depicted in Fig. 8(b), the resulting uncertainty range within the experimental pellet size is around ±1% error for methanol conversion, and ±5% error for CO content at the outlet.

3.3. Impact of experimental heat transfer non-uniformities

Several experimental non-uniformities, first introduced in Section 2.3, could not be resolved or predicted before conducting the experiments. Instead, they are assessed *a posteriori* and included in the model. The modelled non-uniformities are: heat losses to the environment, axial heating variation due to trace heater wrapping density, catalytic bed activity drop, variation of inlet reactant temperature in time, and variation in reactor wall heat capacity. The effects of inlet reactant temperature and wall heat capacity are visible only in the transient state. Their numerical representation and implementation in the model is described in the supplementary material. This subsection discusses the effect of each non-uniformity on the model.

The additions are explored individually for their effects on the steady state temperature profile, as shown in Fig. 9, and conversion and selectivity, shown in Fig. 10. Each addition of experimental non-idealities to the model has a different effect on the process.

The temperature field is most impacted by trace heater wrapping density and bed activity modifications. In terms of conversion and selectivity, the heat losses and bed activity factors have the most influence. In all cases the impact on conversion is small, around 1%, while the CO concentration changes up to 18%. Despite the fact that reaction rates couple the temperature field with conversion and selectivity, their interaction is not entirely obvious to the eye. For example, heat losses addition marginally alter the temperature field but have a high impact on conversion and selectivity. For this reason, all imperfections must apparently be included for accurate predictions of both the temperature field and outlet composition.

The inlet reactant temperature has an evident impact on conversion and selectivity, which is shown in Fig. 11. The outlet CO concentration is directly proportional to the inlet temperature, with each 50

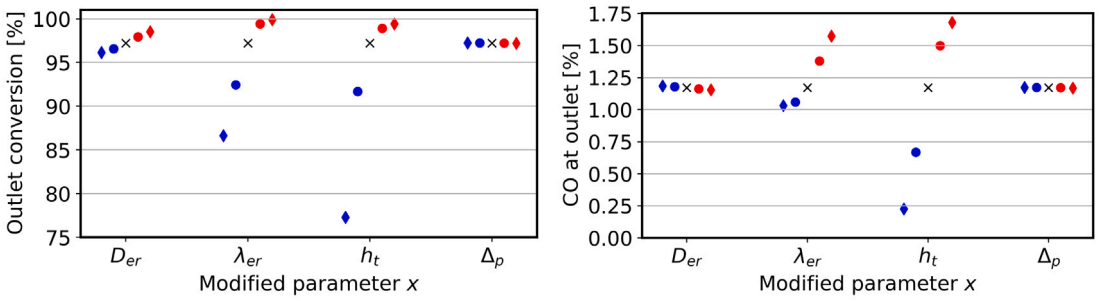

(a) Impact of direct scaling of the selected parameters $D_{er}, \lambda_{er}, h_t$, and Δp.

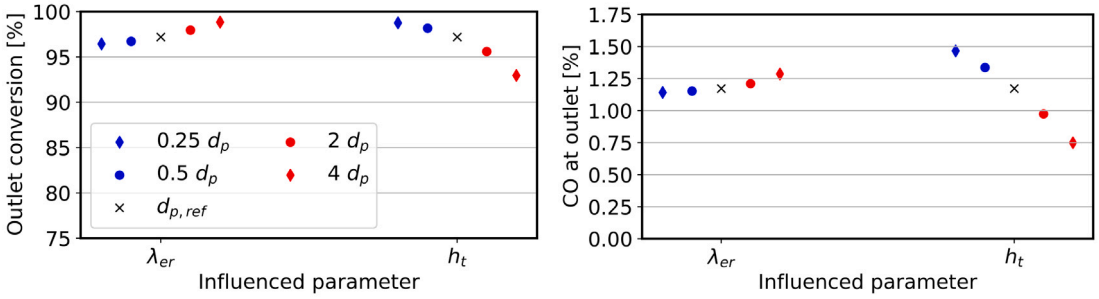

(b) Impact of scaling catalyst average diameter d_p within the expressions for λ_{er} and h_t.

Fig. 8. Sensitivity analysis: impact of scaling selected parameters $D_{er}, \lambda_{er}, h_t$, and Δp; and catalyst average diameter d_p within expressions for λ_{er} and h_t on the outlet conversion and CO concentration; simulation case P = 187 W, $W_{cat.}/F_{CH_3OH}$=200 kg s mol^{-1}.

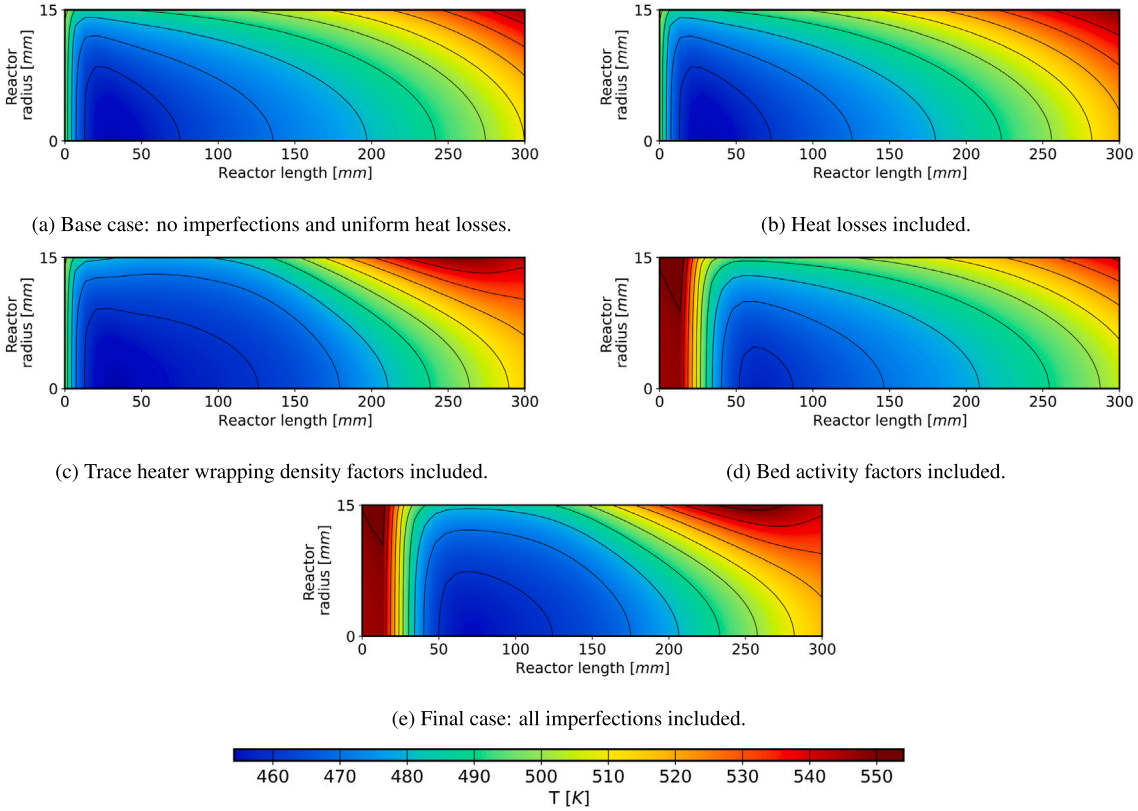

(a) Base case: no imperfections and uniform heat losses.

(b) Heat losses included.

(c) Trace heater wrapping density factors included.

(d) Bed activity factors included.

(e) Final case: all imperfections included.

T [K]

Fig. 9. Isolated effects of each heat non-uniformity inclusion in the simulation on internal reactor temperature field. Simulation case: $W_{cat.}/F_{CH_3OH}$ = 200 kg s mol^{-1}; $P_{el,in}$ = 150 W.

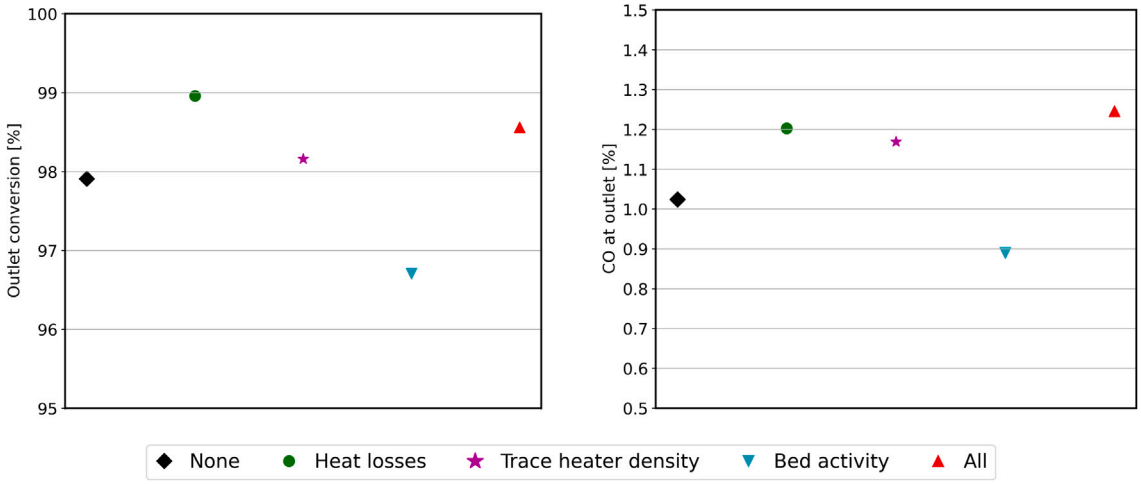

Fig. 10. Isolated effects of heat imperfection modifications in the simulation on outlet conversion and CO content. Simulation case: $W_{cat.}/F_{CH_3OH}$ = 200 kg s mol^{-1}; $P_{el,in}$ = 150 W.

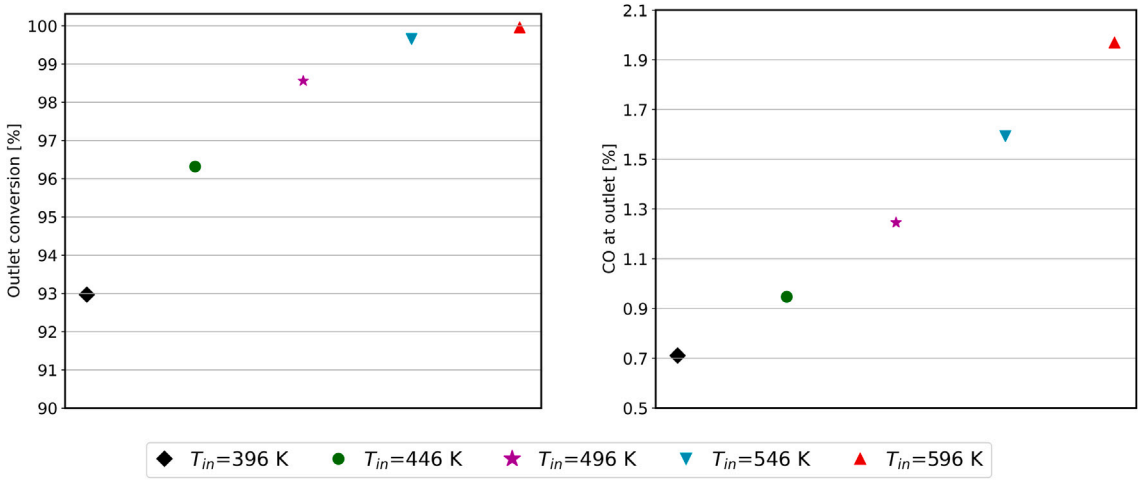

Fig. 11. Effects of inlet reactant temperature varied in 50 K increments in the simulation on outlet conversion and CO content. Simulation case: $W_{cat.}/F_{CH_3OH}$ = 200 kg s mol^{-1}; $P_{el,in}$ = 150 W.

K increment causing ≃0.35% change in CO. The conversion response appears linear up to ≃99%, while its sensitivity decreases as conversion approaches 100%. The inlet temperature in the experiments varies up to 40 K, so its matching further increases simulation accuracy.

Finally, the effects of reactor wall heat capacity factors are only present in transient state. Fig. 12 shows its impact on outlet conversion, produced CO, and internal temperature change in time tracked at reactor outlet. The monitored values move slower towards the new steady state. The wall c_p modification in this case affects the reactor response by increasing its duration to a change in process variable.

4. Experimental validation

All experiments are conducted at outlet pressure p_{out} = 3 bar. Three flows are chosen for the experimental campaign: $W_{cat.}/F_{CH_3OH}$ = 120, 150, 200 kg s mol^{-1}, where $W_{cat.}/F_{CH_3OH}$ is the ratio of catalyst mass to methanol feed rate. The flow specifications are expressed in Table 5. Zhu et al. [35] note that flows lower than $W_{cat.}/F_{CH_3OH}$ = 200 kg s mol^{-1} cause inconsistent experimental CO measurements, possibly due to non-uniform distributions of temperature and species concentration. $W_{cat.}/F_{CH_3OH}$ = 200 kg s mol^{-1} is thus taken as the lower flow boundary in present study. The higher flow boundary of $W_{cat.}/F_{CH_3OH}$ = 120 kg s mol^{-1} is set by the efficiency of evaporator/pre-heater pipe in the experiments. In other words, the inlet reactant temperature is too low at flows higher than $W_{cat.}/F_{CH_3OH}$ = 120 kg s mol^{-1}.

Table 5
Three reactant throughputs used in the experimental campaign, expressed in different flow units.

$W_{cat.}/F_{CH_3OH}$ [kg s mol^{-1}]	120	150	200
Molar CH_3OH flow [mol min^{-1}]	0.37	0.296	0.222
Liquid mixture flow at pump [ml min^{-1}]	9.64	7.712	5.785

Three electrical power heating settings for the reactor are chosen: $P_{el,in}$ = 150, 187, and 224 W. With these heating inputs the internal reactor temperature is kept below 573 K which minimizes catalyst sintering. The methanol conversion in all cases is in the 50%–95% range.

4.1. Steady state validation

The measured and simulated CO concentration in dry reformate gas is reported in Table 6, together with corresponding selected setpoints of heating power and reactant flow. The visualization of CO concentration in Fig. 13 shows that the selectivity trend is matched very well by the

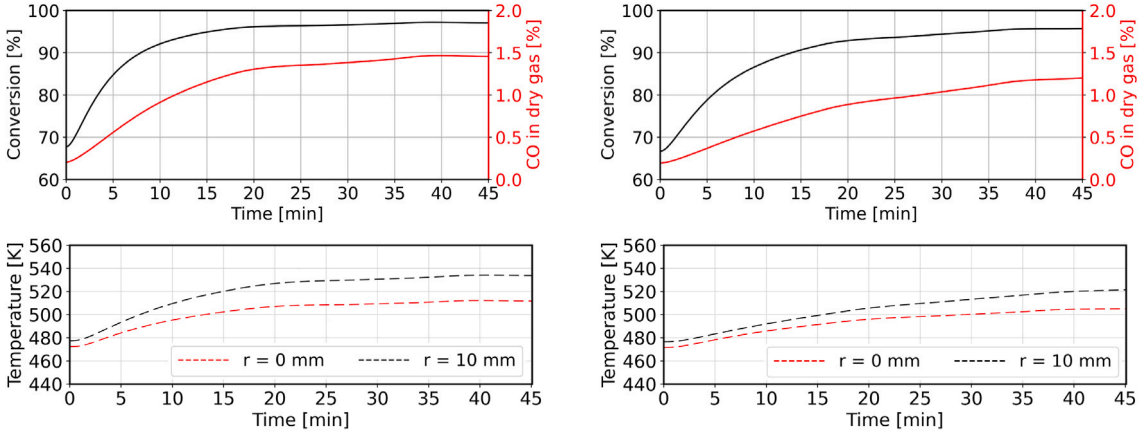

(a) Uniform reactor wall c_p.

(b) Modified reactor wall c_p.

Fig. 12. Effects of reactor wall c_p modification on simulated conversion, CO production, and temperature in time shown at reactor outlet (z = 300 mm). Simulation case: heating power increase of $\Delta P_{el,in}$ = 150–224 W at reactant flow $W_{cat.}/F_{CH_3OH}$ = 150 kg s mol^{-1}.

Table 6
Steady state validation: measured and simulated values of CO in dry reformate gas at different throughput and reactor heating power (p = 3 bar).

El. heating power [W]	$W_{cat.}/F_{CH_3OH}$ [kg s mol^{-1}]	Measured CO in dry gas [mol m^{-3}]	Simulated CO in dry gas [mol m^{-3}]	Simulated CH_3OH conversion [%]
150	120	0.11 - 0.14	0.118	52.83
	150	0.25 - 0.28	0.199	65.53
	200	0.46 - 0.64	0.412	82.33
187	120	0.32 - 0.36	0.315	70.46
	150	0.62 - 0.69	0.615	84.95
	200	1.18 - 1.55	1.356	97.24
224	150	1.26 - 1.45	1.3797	95.28

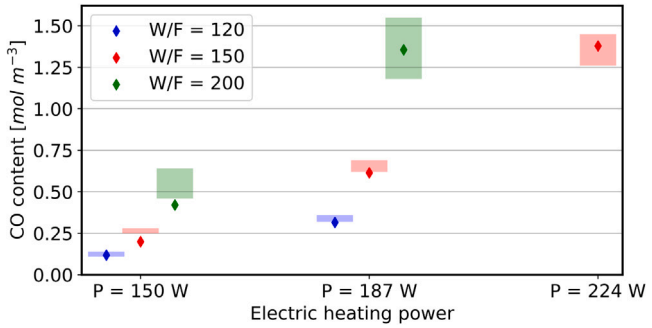

Fig. 13. Steady state validation: graphed measured range of CO in dry reformate gas (transparent rectangles) and simulated values (diamonds) at various inputs of reactor heating and reactant throughput.

simulations. In most cases, the predicted CO concentration is around the lower boundary of measured range.

The pressure sensor precision (±0.1 bar) is too low for conclusive comparison of pressures. The simulated pressure drop values are around Δp = 0.003 bar, while the measurements indicate an average of Δp = 0.05 bar. The consistent low measured Δp values indicate a degree of accuracy. However, due to low precision, pressure values are not used in further validation.

The steady state validation through temperature sensor measurements is shown in Fig. 14. Based on the bed activity, the reactor can be divided into three zones –excluding the low activity zone. The first two zones are heat transfer limited. In the first zone, z < 50 mm the endothermic reactions dominate the heat balance which is seen by rapid decrease of temperature. In the second zone, 50 ≤ z ≤ 150 mm, the heat supply to the reactor is equal to the reaction heat consumption, indicated by the flat temperature profile. This limitation is partly caused by the lower trace heater wrapping density, which is supported by Fig. 9(c). In the third zone, z > 150 mm, the reaction rates slow down due to lower reactant concentrations, causing a temperature increase.

The three distinct reactor zones and their lengths are well captured by the simulations. The simulation is the most accurate in the first two zones, which are highly similar across all cases. In the third zone, the temperature predictions have the highest deviations from experiments, up to 15 K in some cases. The heat balance complexity increases in this zone, since there is not a single dominant heat flux component. The individual terms in the energy equation (Eq. (5)) then have a larger influence over the end result.

The temperature trends are well captured by the simulations and overall accurate, same as with CO content predictions. The simulation precision, namely of the temperature prediction, is likely constrained by uncertainty from heat transfer parameters. For example, the tube side heat transfer coefficient h_t alone is sensitive to catalyst pellet size, and has an evident influence in the overall prediction, as illustrated by the sensitivity study. The validation precision is also expectedly affected by effective radial transport coefficients D_{er} and λ_{er}, omitted axial transport, precision of added heat irregularity factors, measurement accuracy, or other assumptions. The numerical parameters could be fine tuned, if more precision is needed.

4.2. Dynamic validation

The dynamic experiments are performed by observing the reactor response to step changes in input process variables. Reactant flow and

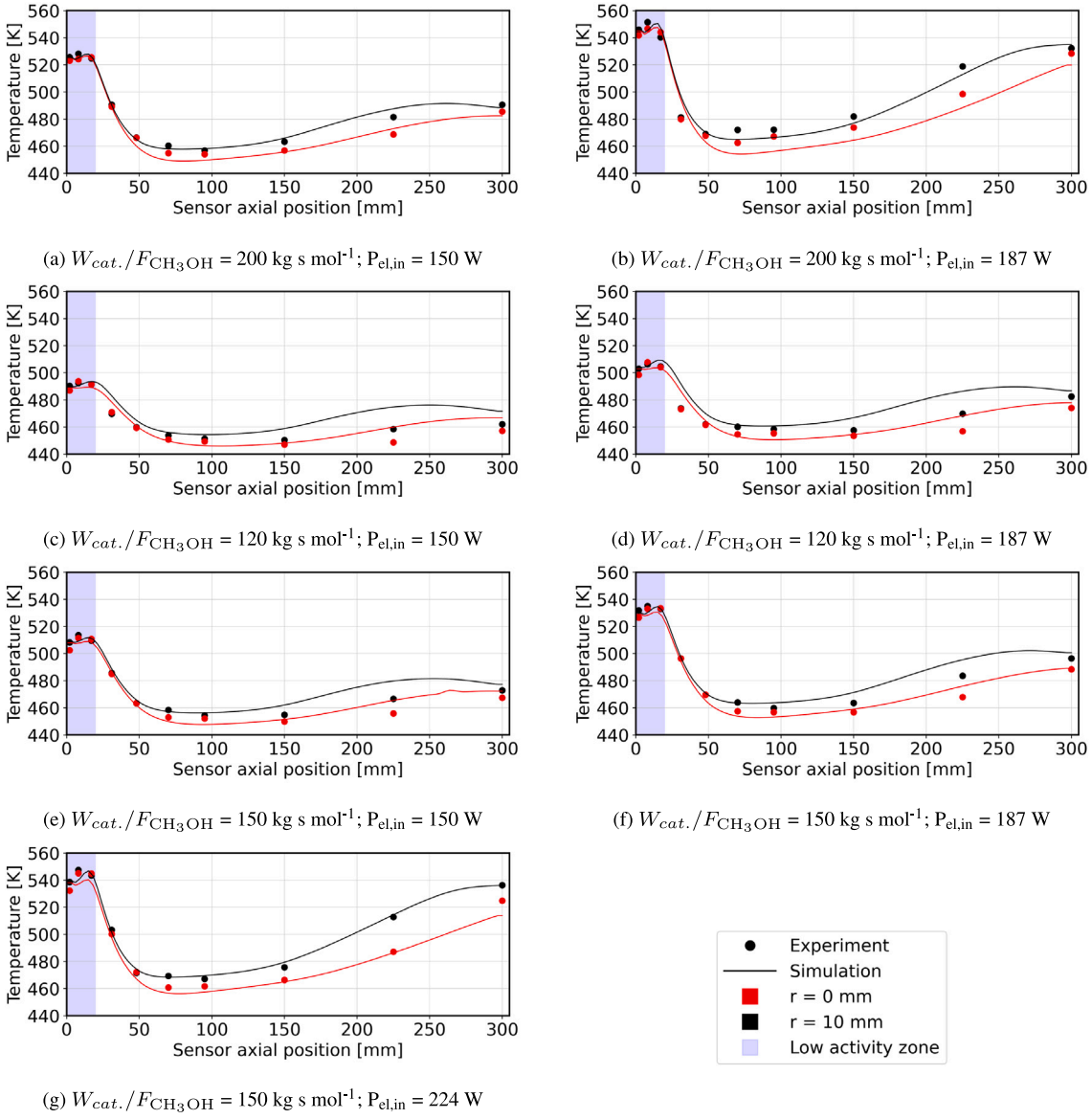

(a) $W_{cat.}/F_{\mathrm{CH_3OH}}$ = 200 kg s mol^{-1}; $P_{el,in}$ = 150 W

(b) $W_{cat.}/F_{\mathrm{CH_3OH}}$ = 200 kg s mol^{-1}; $P_{el,in}$ = 187 W

(c) $W_{cat.}/F_{\mathrm{CH_3OH}}$ = 120 kg s mol^{-1}; $P_{el,in}$ = 150 W

(d) $W_{cat.}/F_{\mathrm{CH_3OH}}$ = 120 kg s mol^{-1}; $P_{el,in}$ = 187 W

(e) $W_{cat.}/F_{\mathrm{CH_3OH}}$ = 150 kg s mol^{-1}; $P_{el,in}$ = 150 W

(f) $W_{cat.}/F_{\mathrm{CH_3OH}}$ = 150 kg s mol^{-1}; $P_{el,in}$ = 187 W

(g) $W_{cat.}/F_{\mathrm{CH_3OH}}$ = 150 kg s mol^{-1}; $P_{el,in}$ = 224 W

Fig. 14. Steady state validation: comparison of experimental and simulated temperature profiles, sampled at different radial and axial positions in the reactor.

Table 7
Variations of flow and heating power in dynamic experiments.

Flow variation experiments		
Set heating power $P_{el,in}$ [W]	Flow increase $W_{cat.}/F_{\mathrm{CH_3OH}}$ [kg s mol^{-1}]	Flow decrease $W_{cat.}/F_{\mathrm{CH_3OH}}$ [kg s mol^{-1}]
150	200 - 120	120 - 200
187	200 - 120	120 - 200
Heat variation experiments		
Set flow $W_{cat.}/F_{\mathrm{CH_3OH}}$ [kg s mol^{-1}]	Heating power increase $P_{el,in}$ [W]	Heating power decrease $P_{el,in}$ [W]
150	150 - 187	187 - 150
150	150 - 224	224 - 150
200	150 - 187	187 - 150

reactor heating power are individually controlled in the experiments, and recorded temperatures are used for model validation. Table 7 shows the changes in reactor inputs used for validation cases.

The results in the main text show selected four cases: one increase and one decrease of flow and heating power each are presented in Figs. 15–18. The focused cases are representative of all explored dynamic cases. The main text figures also put more focus on the comparisons in the second half of the reactor (inserts 9–11), where temperature variations are higher. The first half of the reactor is heat transfer limited, and the temperature variations are generally small. Validation for all sensors in the reactor for a full set of dynamic cases is given in the supplementary material.

In flow increase cases, as illustrated by Fig. 15, the reactor response is characterized by fast initial temperature drop lasting about 5 min.

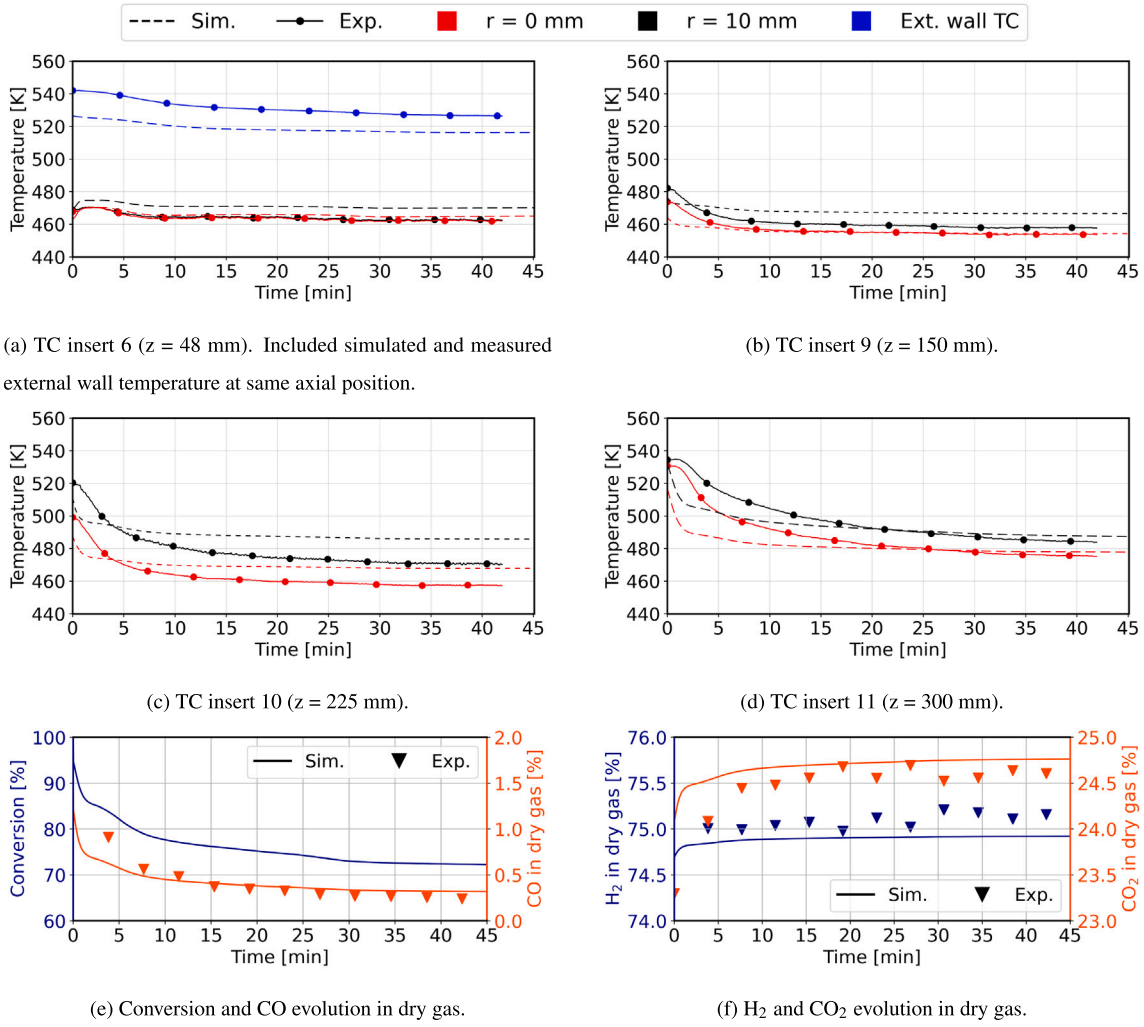

(a) TC insert 6 (z = 48 mm). Included simulated and measured external wall temperature at same axial position.

(b) TC insert 9 (z = 150 mm).

(c) TC insert 10 (z = 225 mm).

(d) TC insert 11 (z = 300 mm).

(e) Conversion and CO evolution in dry gas.

(f) H_2 and CO_2 evolution in dry gas.

Fig. 15. Measured and simulated transient response in temperature and dry gas composition evolution for validation case: reactant flow increase $W_{cat.}/F_{CH_3OH}$ 200–120 kg s mol^{-1} at $P_{el,in}$ = 187 W.

The abruptly higher reaction rates immediately cause a temperature drop within the reactor. This is followed by a slow convergence towards the new value. Flow decrease in Fig. 15 shows that the change is limited at reactor outlet due to the locally higher wall heat capacity. A longer stabilization time is expected in downstream positions. However, the local wall thermal capacity likely has a high influence due to observed differences between flow increase and decrease.

The simulations match the experiments well in regions where the reaction rate is heat transfer limited in flow variation cases. The simulated temperature change is faster than measured near the outlet region. The simulated response is instantaneous, and majority of the change happens within the first two minutes. The following stabilization time is therefore shorter, particularly in the flow increase cases. The simulated temperature change rate then decreases to match more closely with the experiments.

The culprit of simulated fast temperature response is likely in the numerical approach. The pressure and velocity are coupled by the Ergun equation, and the changes are not gradual as in reality, but instantaneous. In the experiments, the flow velocity is affected the back pressure regulator, which in turn is influenced by expanding gas as reactions proceed. This interaction cannot be sufficiently accurately captured by the Ergun equation.

The validations of dry gas composition also show that the experimental selectivity trends are well matched by the simulations. The simulated methanol conversion was calculated by dividing the reacted methanol molar flow by its inlet molar flow: $X_{CH_3OH} = (\dot{n}_{CH_3OH,in} - \dot{n}_{CH_3OH,out})/\dot{n}_{CH_3OH,in}$. The overly fast initial response seen in the temperature comparisons during the first minute is also visible here, particularly in the flow increase case. The trends for H_2, CO_2, and CO concentrations are also predicted well in time.

The variations of reactor heating power produce great matches between simulations and experiments. The trends in Figs. 17 and 18 and their durations are captured by the model in all reactor zones. The simulations shows a more moderate response to heat variations than to flow changes, which also corresponds with the measurements.

The temperature difference between inner (r = 0 mm) and outer (r = 10 mm) thermocouple generally stays similar during transients. In few instances, the difference noticeably varies and the simulation is able to capture it. Figs. 15(d), 17(c), and 18(c) show this agreement. This also suggests the ability for accurate adaptation of effective radial thermal conductivity λ_{er} parameter in time. The outlet dry gas composition closely matches the experimental data in heat variation cases. The trends and predicted values are in excellent agreement with the measurements.

5. Discussion

The dynamic 2D model is successfully validated. The results show the model's ability to reasonably well predict internal temperature in time, and very well predict the CO selectivity in time. The selectivity

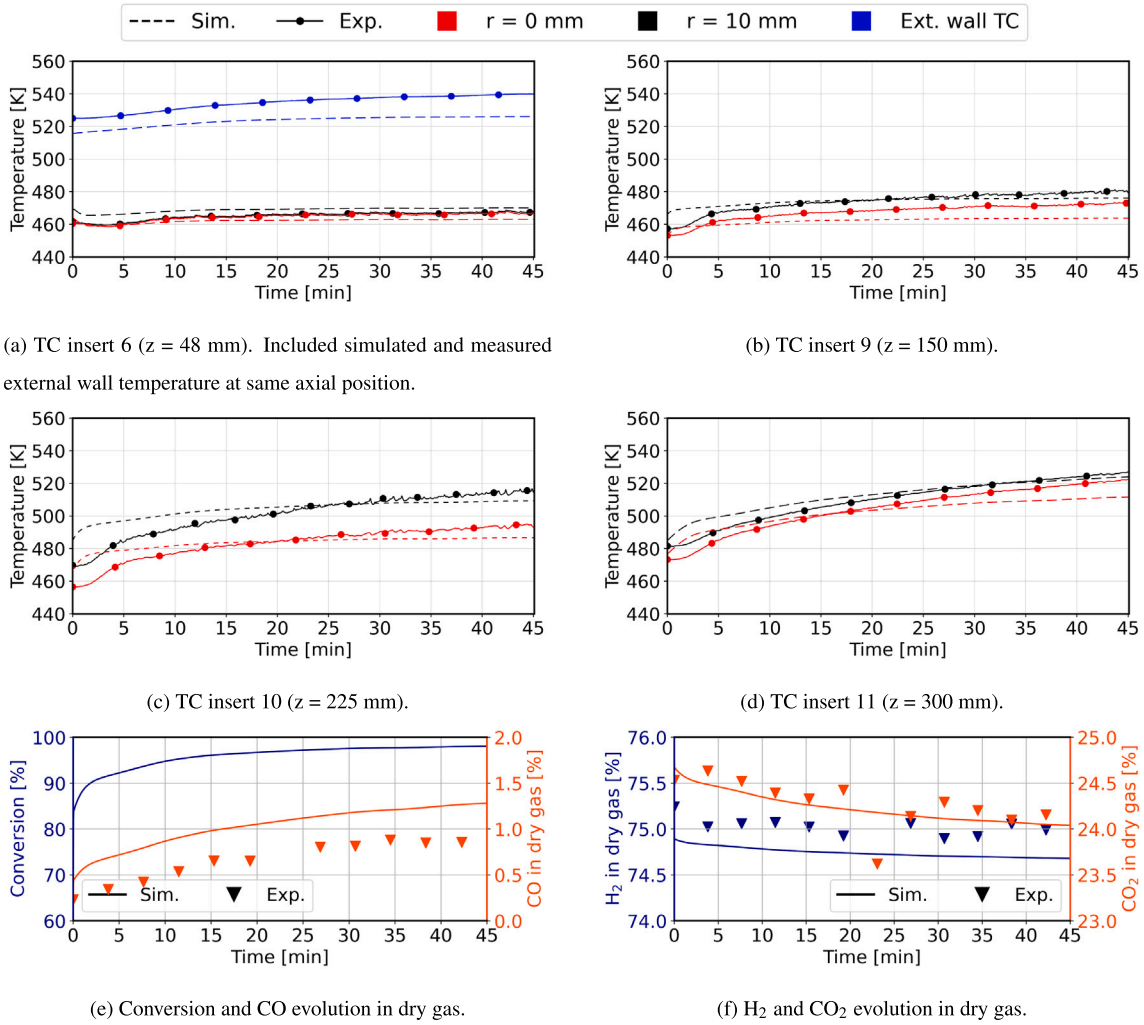

(a) TC insert 6 (z = 48 mm). Included simulated and measured external wall temperature at same axial position.

(b) TC insert 9 (z = 150 mm).

(c) TC insert 10 (z = 225 mm).

(d) TC insert 11 (z = 300 mm).

(e) Conversion and CO evolution in dry gas.

(f) H_2 and CO_2 evolution in dry gas.

Fig. 16. Measured and simulated transient response in temperature and dry gas composition evolution for validation case: reactant flow decrease $W_{cat.}/F_{CH_3OH}$ 120–200 kg s mol^{-1} at $P_{el,in}$ = 187 W.

in time is the most critical parameter for reformer combination with PEM fuel cells. The model is therefore applicable for unsteady reactor design tasks.

The present study foremost exposes the high influence of external heat transfer non-uniformities on reactor performance in both steady and transient regimes. The experimental measurements can be significantly clouded by various practical elements, which could be present on larger scales as well. The reactor-specific heat transfer characteristics can also affect the model precision. These characteristics in their effect proved to be as important as the choice of numerical correlations. The resulting implication is that the reactor design procedures should account for external heat transfer features.

Traditional tube-in-shell heat exchangers have multiple potential sources of heat supply non-uniformities. In steady state operation heat losses alter the flue gas temperature, which affects the heat supply for the reactions. Maintaining a steady inlet feed temperature can be challenging in practice, which affects both steady and dynamic reactor operation. The transient predictions may be affected by local variations of wall c_p caused by the baffle plates that support the tube bundles. These non-uniformities warrant further investigation into gravity of their effect in practice.

A key element in the presently used numerical model are the numerous sources of uncertainty. First are the multiple added modification factors for validation. They cannot be directly measured, and in this study are instead produced iteratively. The second source are a number of used semi-empirical correlations. This is amplified by the 2D pseudo-homogeneous nature of the model which introduces effective parameters such as D_{er} and λ_{er}. Third are the assumed uniformities in the model that are not necessarily true in reality. These are catalyst pellet size, ideal interfaces between active and passive zones, and uniform bed packing density which in reality is locally altered by the thermocouple inserts. The model agrees with measurements despite all assumptions. It is also likely that the assumptions are valid outside of the investigated parameter range, but the range of its validity is uncertain.

The present validity range is determined by process variables and reactor geometry. Since process variables were determined by the equipment capabilities, both aspects require a different experimental setup(s) to quantify the validity range. With respect to geometry, the uncertainty is situated in the effective radial transport parameters. Moghaddam et al. [42] show a dependency of λ_{er} on the reactor length. Moreover, the present study readily assumes that expressions for D_{er}, λ_{er}, h_t are valid in the transient regime. The assumption holds true in the present case, but it should ideally be explored individually in a separate study.

The invasive measurement technique with sensor inserts was expectedly shown problematic in practice. Radial insertion of multiple inserts at the zone of interest alters the zone activity and its heating. Alternatively, the sensors can be inserted in the axial direction. The bed packing is then uniform in axial direction, outer reactor surface is

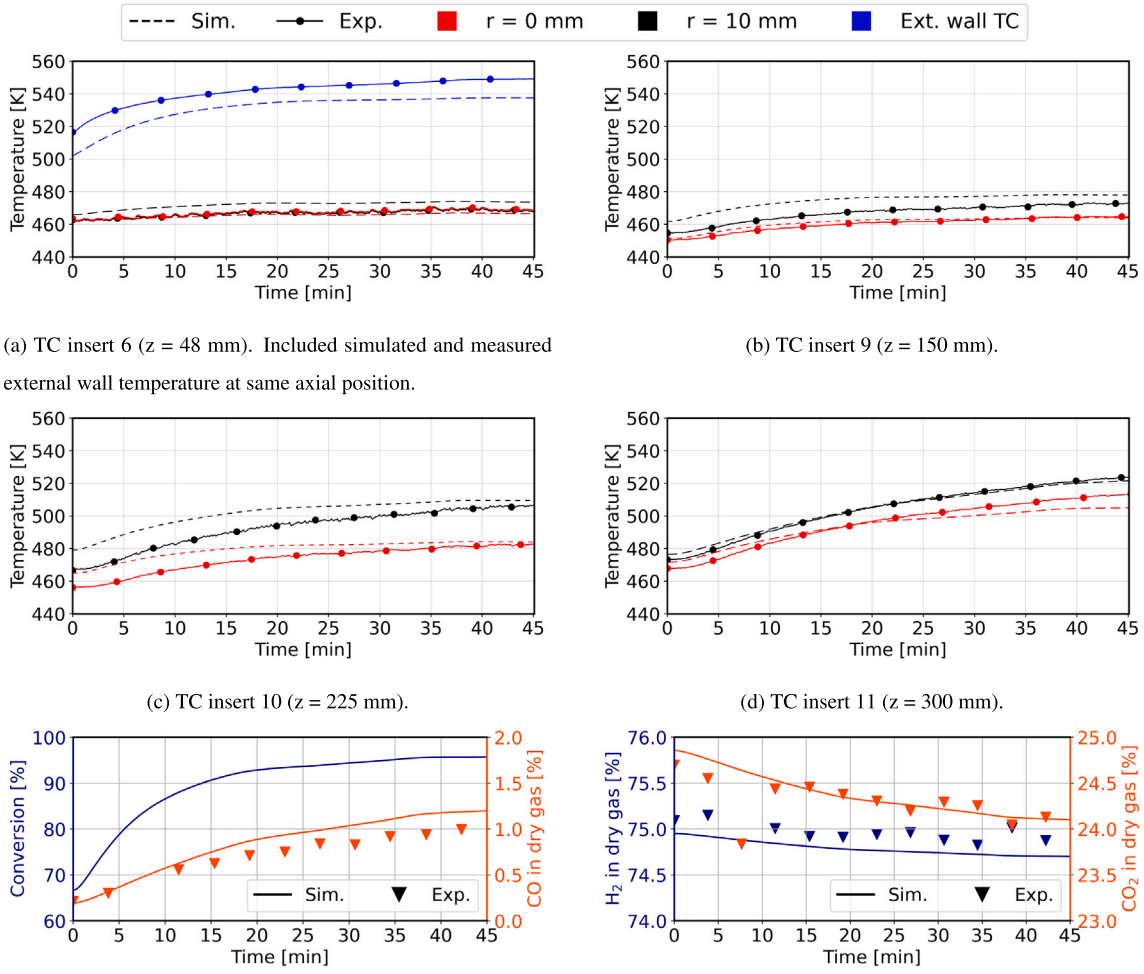

(a) TC insert 6 (z = 48 mm). Included simulated and measured external wall temperature at same axial position.

(b) TC insert 9 (z = 150 mm).

(c) TC insert 10 (z = 225 mm).

(d) TC insert 11 (z = 300 mm).

(e) Conversion and CO evolution in dry gas.

(f) H_2 and CO_2 evolution in dry gas.

Fig. 17. Measured and simulated transient response in temperature and dry gas composition evolution for validation case: heating increase $P_{el,in}$ 150–224 W at $W_{cat.}/F_{CH_3OH}$ = 150 kg s mol^{-1}.

smooth, and heat conduction along the insert is decreased. However, axial inserts are significantly longer and likely thicker. They can bend more easily, or if they are thicker, displace enough catalyst to locally decrease the activity. Experimentally it is also difficult to precisely control individual parameters. For these reasons, suggested alternative approach is validation via high fidelity CFD models.

The follow-up to this work would be reactor scale-up, with the experimental part as the main hurdle. Experimental validation at larger scale should employ steam or flue-gas heating in a tube-and-shell heat exchanger. This would enable the study of industrially relevant thermal non-uniformities. On the modelling side, scale-up remains computationally efficient under the common assumption of identical tube behaviour. This is done by again simulating a single representative tube and preserves the existing model structure. The approach is demonstrated in the original steady state model [36]. The validity of identical tube behaviour could be further investigated, but requires a dedicated experimental study.

Finally, the present study occupies a distinct position within the fixed bed reactor literature. Some conclusions are shared with previous laboratory-scale experimental studies such as the importance of heat losses in experiments and modelling [43,44], and noted influence of invasive measurement techniques [45]. The difference from previous studies stems from the primary objectives which is typically centred on process intensification [44,46], scale-up [44,45,47], or the effects of reactor geometry and operating conditions [43,45,48]. In contrast, the present work is explicitly aimed at demonstrating that a practical level of model fidelity can reliably support unsteady reactor design. This contribution extends beyond the validation of a particular model. The study establishes and validates a general methodology for developing predictive reactor models, providing a framework that can be transferred to a wide range of fixed-bed reactor systems and reaction chemistries.

6. Conclusions and outlook

A dynamic 2D pseudo-homogeneous model for methanol steam reforming in a fixed bed reactor was presented and experimentally validated against temperature and CO concentration data. The developed model is an efficient contribution to the design toolkit of reactor designers for fixed bed reactors in transient regimes. The study shows that capturing external heat transfer effects is critical in validation studies. Their inclusion in reactor design tasks is also recommended, if known to the designer. The presented model has a relatively large number of parameters with uncertainty. The 2D model was shown valid for transient predictions. The validity outside of the explored geometry and process variable space may be strengthened with further experiments.

The used invasive experimental techniques proved effective, but have shortcomings. Sensor inserts interfered with the packed bed and reactor heating, and their presence influenced the measured data.

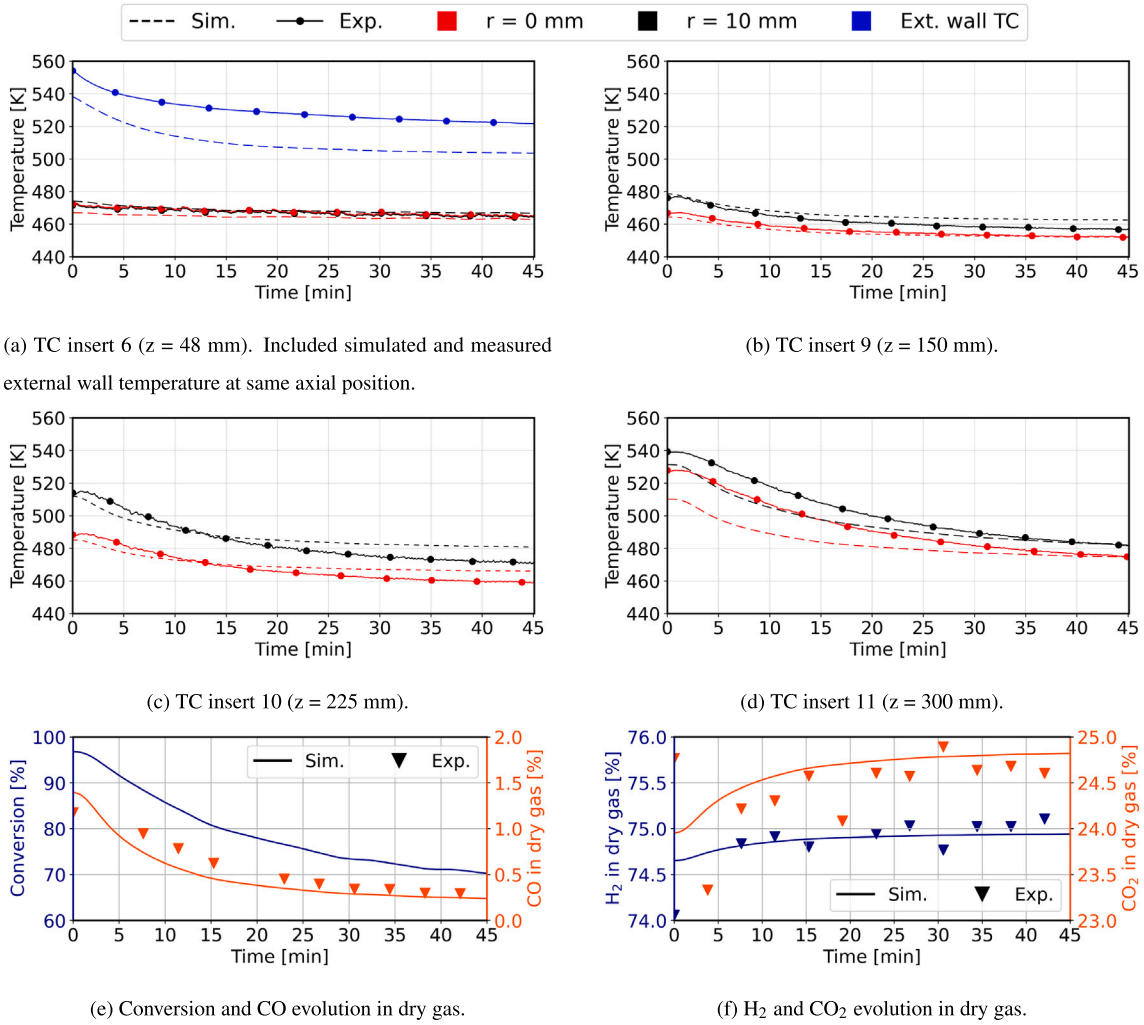

(a) TC insert 6 (z = 48 mm). Included simulated and measured external wall temperature at same axial position.

(b) TC insert 9 (z = 150 mm).

(c) TC insert 10 (z = 225 mm).

(d) TC insert 11 (z = 300 mm).

(e) Conversion and CO evolution in dry gas.

(f) H_2 and CO_2 evolution in dry gas.

Fig. 18. Measured and simulated transient response in temperature and dry gas composition evolution for validation case: heating decrease $P_{el,in}$ 224–150 W at $W_{cat.}/F_{CH_3OH}$ = 150 kg s mol^{-1}.

The interferences were individually identified, presented, and then addressed a posteriori in the model. The invasive approach is thus not recommended for future studies, unless no other approach is possible. Alternatively, CFD based approach is possible for validations using detailed transient internal flow field variables.

The transient characteristics were adequately captured by the model, most accurately in cases with reactor heating manipulation. The model is therefore fit for transient reactor design tasks in methanol steam reforming. By modifying reaction kinetics the study also becomes relevant to other on-demand chemical conversion processes in packed bed reactors, positively helping usher in a hydrogen based future.

CRediT authorship contribution statement

Bojan Grenko: Writing – review & editing, Writing – original draft, Visualization, Validation, Software, Methodology, Investigation, Formal analysis, Data curation, Conceptualization. **Lindert van Biert:** Writing – review & editing, Supervision, Resources, Project administration, Methodology, Investigation, Funding acquisition, Formal analysis, Conceptualization. **Robert van de Ketterij:** Writing – review & editing, Supervision, Investigation, Formal analysis. **Wiebren de Jong:** Writing – review & editing, Supervision, Resources, Investigation, Formal analysis, Conceptualization.

Declaration of competing interest

The authors declare that they have no known competing financial interests or personal relationships that could have appeared to influence the work reported in this paper.

Acknowledgements

The present work is part of the MENENS project, funded by the Netherlands Enterprise Agency (RVO: Rijksdienst voor Ondernemend Nederland) under the grant number MOB21012.

Appendix A. Supplementary data

Supplementary material related to this article can be found online at https://doi.org/10.1016/j.cej.2026.179613.

Data availability

Data will be made available on request.

References

[1] H. Durak, Comprehensive assessment of thermochemical processes for sustainable waste management and resource recovery, Processes 11 (7) (2023) 2092, http://dx.doi.org/10.3390/pr11072092.

[2] Y. Yao, K. Lan, T.E. Graedel, N.D. Rao, Models for decarbonization in the chemical industry, Annu. Rev. Chem. Biomol. Eng. 15 (1) (2024) 139–161, http://dx.doi.org/10.1146/annurev-chembioeng-100522-114115.

[3] T. Maunula, K. Kallinen, T. Wolff, M. Mikulski, Catalytic aftertreatment systems for combustion exhaust gases from future hydrogen, ammonia and e-HC engines, Top. Catal. 68 (20) (2025) 2565–2580, http://dx.doi.org/10.1007/s11244-025-02131-x.

[4] A. Olabi, T. Wilberforce, K. Elsaid, E.T. Sayed, H.M. Maghrabie, M.A. Abdelkareem, Large scale application of carbon capture to process industries – a review, J. Clean. Prod. 362 (2022) 132300, http://dx.doi.org/10.1016/j.jclepro.2022.132300.

[5] C.d.S. Cachola, M. Ciotta, A. Azevedo dos Santos, D. Peyerl, Deploying of the carbon capture technologies for CO2 emission mitigation in the industrial sectors, Carbon Capture Sci. Technol. 7 (2023) 100102, http://dx.doi.org/10.1016/j.ccst.2023.100102.

[6] E. Enasel, G. Dumitrascu, Storage solutions for renewable energy: A review, Energy Nexus 17 (2025) 100391, http://dx.doi.org/10.1016/j.nexus.2025.100391.

[7] V. Mahadevan, S.R. S, M.A. Rusho, S. Yishak, Critical review of energy storage systems: A comparative assessment of mechanisms, advantages, challenges, and integration with renewable energy, Results Eng. 26 (2025) 105589, http://dx.doi.org/10.1016/j.rineng.2025.105589.

[8] R. Hren, A. Vujanović, Y. Van Fan, J.J. Klemeš, D. Krajnc, L. Čuček, Hydrogen production, storage and transport for renewable energy and chemicals: An environmental footprint assessment, Renew. Sustain. Energy Rev. 173 (2023) 113113, http://dx.doi.org/10.1016/j.rser.2022.113113.

[9] N.A.A. Qasem, G.A.Q. Abdulrahman, A recent comprehensive review of fuel cells: History, types, and applications, Int. J. Energy Res. 2024 (1) (2024) 7271748, http://dx.doi.org/10.1155/2024/7271748.

[10] Y. Luo, Y. Wu, B. Li, T. Mo, Y. Li, S.-P. Feng, J. Qu, P.K. Chu, Development and application of fuel cells in the automobile industry, J. Energy Storage 42 (2021) 103124, http://dx.doi.org/10.1016/j.est.2021.103124.

[11] L. van Biert, K. Visser, Fuel cells systems for sustainable ships, in: Sustainable Energy Systems on Ships, Elsevier, 2022, pp. 81–121, http://dx.doi.org/10.1016/b978-0-12-824471-5.00010-4.

[12] T.H. Ulucan, S.A. Akhade, A. Ambalakatte, T. Autrey, A. Cairns, P. Chen, Y.W. Cho, F. Gallucci, W. Gao, J.B. Grinderslev, K. Grubel, T.R. Jensen, P.E. de Jongh, J. Kothandaraman, K.E. Lamb, Y.-S. Lee, C. Makhloufi, P. Ngene, P. Olivier, C.J. Webb, B. Wegman, B.C. Wood, C. Weidenthaler, Hydrogen storage in liquid hydrogen carriers: recent activities and new trends, Prog. Energy 5 (1) (2023) 012004, http://dx.doi.org/10.1088/2516-1083/acac5c.

[13] E. Pawelczyk, N. Ł ukasik, I. Wysocka, A. Rogala, J. Gębicki, Recent progress on hydrogen storage and production using chemical hydrogen carriers, Energies 15 (14) (2022) 4964, http://dx.doi.org/10.3390/en15144964.

[14] S. Qian, H. Zhou, D. Mei, Y. Wang, Development of integrated thermally autonomous reformed methanol-proton exchange membrane fuel cell system, J. Power Sources 624 (2024) 235536, http://dx.doi.org/10.1016/j.jpowsour.2024.235536.

[15] Y. Ma, Z. Wang, H. Liu, H. Tang, Y. Ji, F. Han, Efficient and sustainable power propulsion for all-electric ships: An integrated methanol-fueled SOFC-sCO2 system, Renew. Energy 230 (2024) 120822, http://dx.doi.org/10.1016/j.renene.2024.120822.

[16] B. Hu, P. Xu, L. Wang, D. Xiang, F. Jiang, D. Cao, K. Liu, Stability analysis and multi-objective optimization of methanol steam reforming for on-line hydrogen production, Int. J. Hydrog. Energy 91 (2024) 434–446, http://dx.doi.org/10.1016/j.ijhydene.2024.09.342.

[17] L.J.R. Nunes, Renewable methanol as an agent for the decarbonization of maritime logistic systems: A review, Futur. Transp. 5 (2) (2025) 54, http://dx.doi.org/10.3390/futuretransp5020054.

[18] B. Grenko, W. de Jong, R. van de Ketterij, L. van Biert, Analytical and numerical aspects of dynamic industrial chemical process analysis in fixed bed reactors, Chem. Eng. Sci. 325 (2026) 123421, http://dx.doi.org/10.1016/j.ces.2026.123421.

[19] C. Xu, F. Ju, X. Zheng, Y. Liu, J. Huang, G. Li, Y. Li, L. Zhu, L. Ye, H. Pan, Computational fluid dynamics modelling of fixed-bed reactors using particle-resolved approach, Processes 13 (6) (2025) 1820, http://dx.doi.org/10.3390/pr13061820.

[20] J. Zhu, Z. Yuan, L. Wang, C. Dong, J. Lu, J. Ding, 3D simulation in a fixed bed coupled pervaporation reactor for biodiesel production, Chem. Eng. J. 496 (2024) 153854, http://dx.doi.org/10.1016/j.cej.2024.153854.

[21] E.A. Daymo, M. Hettel, Fixed bed reactor modeling with internal and external transport resistances: Comparing 3D PRCFD and 2D porous media simulations, Chem. Eng. Sci. 321 (2026) 122779, http://dx.doi.org/10.1016/j.ces.2025.122779.

[22] A.M. Ranjekar, G.D. Yadav, Steam reforming of methanol for hydrogen production: A critical analysis of catalysis, processes, and scope, Ind. Eng. Chem. Res. 60 (2021) 89–113, http://dx.doi.org/10.1021/acs.iecr.0c05041.

[23] N. Li, X. Cui, J. Zhu, M. Zhou, V. Liso, G. Cinti, S.L. Sahlin, S.S. Araya, A review of reformed methanol-high temperature proton exchange membrane fuel cell systems, Renew. Sustain. Energy Rev. 182 (2023) 113395, http://dx.doi.org/10.1016/j.rser.2023.113395.

[24] A. Lotrič, M. Sekavčnik, S. Hočevar, Effectiveness of heat-integrated methanol steam reformer and polymer electrolyte membrane fuel cell stack systems for portable applications, J. Power Sources 270 (2014) 166–182, http://dx.doi.org/10.1016/j.jpowsour.2014.07.072, URL https://www.sciencedirect.com/science/article/pii/S0378775314011161.

[25] Y. Wang, Q. Wu, D. Mei, Y. Wang, Development of highly efficient methanol steam reforming system for hydrogen production and supply for a low temperature proton exchange membrane fuel cell, Int. J. Hydrog. Energy 45 (46) (2020) 25317–25327, http://dx.doi.org/10.1016/j.ijhydene.2020.06.285, URL https://www.sciencedirect.com/science/article/pii/S0360319920324952.

[26] P. Ribeirinha, M. Abdollahzadeh, J.M. Sousa, M. Boaventura, A. Mendes, Modelling of a high-temperature polymer electrolyte membrane fuel cell integrated with a methanol steam reformer cell, Appl. Energy 202 (2017) 6–19, http://dx.doi.org/10.1016/J.APENERGY.2017.05.120.

[27] G. Garcia, E. Arriola, W.H. Chen, M.D.D. Luna, A comprehensive review of hydrogen production from methanol thermochemical conversion for sustainability, Energy 217 (2021) 119384, http://dx.doi.org/10.1016/J.ENERGY.2020.119384.

[28] G. Towler, R. Sinnott, Heat transfer equipment, in: Chemical Engineering Design, Elsevier, 2022, pp. 823–951, http://dx.doi.org/10.1016/b978-0-12-821179-3.00019-4.

[29] G. Eigenberger, W. Ruppel, Catalytic fixed-bed reactors, ISBN: 9783527306732, 2012.

[30] M. Idamakanti, E.B. Ledesma, R.R. Ratnakar, M.P. Harold, V. Balakotaiah, P. Bollini, Electrified catalysts for endothermic chemical processes: Materials needs, advances, and challenges, ACS Eng. Au 4 (1) (2023) 71–90, http://dx.doi.org/10.1021/acsengineeringau.3c00051.

[31] M. Zhang, D. Liu, Y. Wang, L. Zhao, G. Xu, Y. Yu, H. He, Recent advances in methanol steam reforming catalysts for hydrogen production, Catalysts 15 (1) (2025) 36, http://dx.doi.org/10.3390/catal15010036.

[32] B. Grenko, W. de Jong, R. van de Ketterij, L. van Biert, Dynamic modelling of methanol steam reforming to hydrogen in a packed bed reactor for shipboard fuel cells, Chem. Eng. J. 507 (2025) 160623, http://dx.doi.org/10.1016/j.cej.2025.160623, URL https://www.sciencedirect.com/science/article/pii/S1385894725014445.

[33] T. Eppinger, N. Jurtz, M. Kraume, Influence of macroscopic wall structures on the fluid flow and heat transfer in fixed bed reactors with small tube to particle diameter ratio, Processes 9 (4) (2021) 689, http://dx.doi.org/10.3390/pr9040689.

[34] J. Zhu, S.S. Araya, X. Cui, S.L. Sahlin, S.K. Kæ r, Modeling and design of a multi-tubular packed-bed reactor for methanol steam reforming over a Cu/ZnO/Al2O3 catalyst, Energies 13 (3) (2020) http://dx.doi.org/10.3390/en13030610, URL https://www.mdpi.com/1996-1073/13/3/610.

[35] J. Zhu, X. Cui, S.S. Araya, Comparison between 1D and 2D numerical models of a multi-tubular packed-bed reactor for methanol steam reforming, Int. J. Hydrog. Energy 47 (54) (2022) 22704–22719, http://dx.doi.org/10.1016/j.ijhydene.2022.05.109, URL https://www.sciencedirect.com/science/article/pii/S0360319922021474.

[36] J. Zhu, Modelling of a packed-bed methanol steam reformer for HT-PEM fuel cell applications, in: Ph.D.-serien for Det Ingeniør- og Naturvidenskabelige Fakultet, Aalborg Universitet, Aalborg Universitetsforlag, 2022, http://dx.doi.org/10.54337/aau513444640.

[37] B. Grenko, Methanol steam reformer code git repository, 2025, http://dx.doi.org/10.5281/ZENODO.16941636.

[38] J. Zhu, S.S. Araya, X. Cui, S.K. Kæ r, The role of effectiveness factor on the modeling of methanol steam reforming over CuO/ZnO/Al2O3 catalyst in a multi-tubular reactor, Int. J. Hydrog. Energy 47 (14) (2022) 8700–8715, http://dx.doi.org/10.1016/j.ijhydene.2021.12.223.

[39] M. Sahimi, Dispersion in flow through porous media, in: Flow and Transport in Porous Media and Fractured Rock, John Wiley & Sons, Ltd, 2011, pp. 341–413, http://dx.doi.org/10.1002/9783527636693.ch11.

[40] B.A. Peppley, J.C. Amphlett, L.M. Kearns, R.F. Mann, Methanol–steam reforming on Cu/ZnO/Al2O3 catalysts. part 2. a comprehensive kinetic model, Appl. Catal. A: Gen. 179 (1999) 31–49, http://dx.doi.org/10.1016/S0926-860X(98)00299-3.

[41] H.S. Fogler, Elements of Chemical Reaction Engineering, fourth ed., Prentice Hall, 2005.

[42] E. Moghaddam, E. Foumeny, A. Stankiewicz, J. Padding, Multiscale modelling of wall-to-bed heat transfer in fixed beds with non-spherical pellets: From particle-resolved CFD to pseudo-homogenous models, Chem. Eng. Sci. 236 (2021) 116532, http://dx.doi.org/10.1016/j.ces.2021.116532.

[43] K. Risthaus, I. Bürger, M. Linder, M. Schmidt, Numerical analysis of the hydration of calcium oxide in a fixed bed reactor based on lab-scale experiments, Appl. Energy 261 (2020) 114351, http://dx.doi.org/10.1016/j.apenergy.2019.114351.

[44] V.S. Ermolaev, K.O. Gryaznov, E.B. Mitberg, V.Z. Mordkovich, V.F. Tretyakov, Laboratory and pilot plant fixed-bed reactors for Fischer–Tropsch synthesis: Mathematical modeling and experimental investigation, Chem. Eng. Sci. 138 (2015) 1–8, http://dx.doi.org/10.1016/j.ces.2015.07.036.

[45] J.F. Pérez, A. Melgar, F.V. Tinaut, Modeling of fixed bed downdraft biomass gasification: Application on lab-scale and industrial reactors: Modeling of fixed bed downdraft biomass gasification, Int. J. Energy Res. 38 (3) (2013) 319–338, http://dx.doi.org/10.1002/er.3045.

[46] B. Dou, H. Zhang, G. Cui, Z. Wang, B. Jiang, K. Wang, H. Chen, Y. Xu, Hydrogen production by sorption-enhanced chemical looping steam reforming of ethanol in an alternating fixed-bed reactor: Sorbent to catalyst ratio dependencies, Energy Convers. Manage. 155 (2018) 243–252, http://dx.doi.org/10.1016/j.enconman.2017.10.075.

[47] V. Spallina, B. Marinello, F. Gallucci, M. Romano, M. Van Sint Annaland, Chemical looping reforming in packed-bed reactors: Modelling, experimental validation and large-scale reactor design, Fuel Process. Technol. 156 (2017) 156–170, http://dx.doi.org/10.1016/j.fuproc.2016.10.014.

[48] G. Chabot, R. Guilet, P. Cognet, C. Gourdon, A mathematical modeling of catalytic milli-fixed bed reactor for Fischer–Tropsch synthesis: Influence of tube diameter on Fischer Tropsch selectivity and thermal behavior, Chem. Eng. Sci. 127 (2015) 72–83, http://dx.doi.org/10.1016/j.ces.2015.01.015.